

Electrical Conductivity and Photodetection in 3D-Printed Nanoporous Structures via Solution-Processed Functional Materials

Kai Xia, Zheqin Dong, Qing Sun, Rafaela Debastiani, Sida Liu, Qihao Jin, Yang Li, Ulrich W. Paetzold, Peter Gumbsch, Uli Lemmer, Yolita M. Eggeler, Pavel A. Levkin, and Gerardo Hernandez-Sosa*

3D-printed conductive structures are highly attractive due to their great potential for customizable electronic devices. While the traditional 3D printing of metal requires high temperatures to sinter metal powders or polymer/metal composites, low or room temperature processes will be advantageous to enable multi-material deposition and integration of optoelectronic applications. Herein, digital light processing technology and inkjet printing are combined as an effective strategy to fabricate customized 3D conductive structures. In this approach, a 3D-printed nanoporous (NPo) polymeric material is used as a substrate onto which a nanoparticle-based Ag ink is printed. SEM and X-ray nano computed tomography (nanoCT) measurements show that the porous morphology of the pristine NPo is retained after deposition and annealing of the Ag ink. By optimizing the deposition conditions, conductive structures with sheet resistance $<2 \Omega \text{ sq}^{-1}$ are achieved when annealing at temperatures as low as 100 °C. Finally, the integration of an inkjet-printed photodetector is investigated based on an organic semiconductor active layer onto the NPo substrate. Thus, the potential of this approach is demonstrated for the additive manufacturing of functional 3D-printed optoelectronic devices.

1. Introduction

3D printing as an additive manufacturing technique has developed significantly in recent years, from thermoplastic printing to light-assisted printing techniques.^[1–4] One of the current challenges in these research fields is to realize the printing of 3D electrically conductive structures which could be compatible with the fabrication of devices such as batteries, and wireless sensors and their integration into electronic circuits.^[5–8] One of the established ways to fabricate a 3D conductive structure is using a high-power laser or an electron beam to layer-by-layer melt and/or sinter a metal (i.e., alloy) powder.^[9,10] However, this manufacturing technique requires processing temperatures $\geq 900 \text{ °C}$, which can complicate the development of integrative processes.^[1,11] An alternative solution to process 3D-printed conductive materials is the use of liquid

K. Xia, Q. Jin, Y. Li, U. W. Paetzold, U. Lemmer, G. Hernandez-Sosa
Light Technology Institute (LTI)
Karlsruhe Institute of Technology (KIT)
Engesserstrasse 13, 76131 Karlsruhe, Germany
E-mail: gerardo.sosa@kit.edu

K. Xia, U. Lemmer, G. Hernandez-Sosa
InnovationLab
Speyerer Strasse 4, 69115 Heidelberg, Germany

Z. Dong, S. Liu, P. A. Levkin
Institute of Biological and Chemical Systems – Functional Molecular
Systems (IBCS-FMS)
Karlsruhe Institute of Technology (KIT)
Hermann-von-Helmholtz-Platz 1, 76344 Eggenstein-Leopoldshafen,
Germany

Z. Dong, S. Liu, P. A. Levkin
Institute of Organic Chemistry (IOC)
Karlsruhe Institute of Technology (KIT)
Kaiserstrasse 12, 76131 Karlsruhe, Germany

Q. Sun, Y. M. Eggeler
Microscopy of Nanoscale Structures & Mechanisms (MNM)
Laboratory for Electron Microscopy (LEM)
Karlsruhe Institute of Technology (KIT)
Engesserstrasse 7, 76131 Karlsruhe, Germany

R. Debastiani, P. Gumbsch
Institute of Nanotechnology (INT)
Karlsruhe Institute of Technology (KIT)
Hermann-von-Helmholtz-Platz 1, 76344 Eggenstein-Leopoldshafen,
Germany

 The ORCID identification number(s) for the author(s) of this article can be found under <https://doi.org/10.1002/admt.202300408>

© 2023 The Authors. Advanced Materials Technologies published by Wiley-VCH GmbH. This is an open access article under the terms of the Creative Commons Attribution License, which permits use, distribution and reproduction in any medium, provided the original work is properly cited.

DOI: 10.1002/admt.202300408

metals, such as gallium alloys, due to their low melting points.^[12,13] By changing their composition, their properties can be tuned to an appropriate range compatible with 3D printing technology, however, due to their soft nature the structure can be deformed or even completely lost if touched or squeezed.^[13,14] Acoustophoretic printing has enabled scientists to print eutectic gallium–indium (eGaIn, $T_{\text{melting}} = 15.7\text{ }^{\circ}\text{C}$) into a self-supporting 3D structure at room temperature with a resolution of $\approx 200\text{ }\mu\text{m}$.^[13,15] In another example, Park et al. utilized 3D direct printing to fabricate durable 3D structures with a minimum line width of $5\text{ }\mu\text{m}$ with a composite comprising eGaIn and carbon nanotube decorated with platinum (Pt) nanoparticles. The materials exhibited low resistance of $\approx 10\text{ }\Omega$ however required annealing at $340\text{ }^{\circ}\text{C}$ to preserve their shape after printing.^[16] In addition to using liquid metals, nanoparticle-based inks present an opportunity for solution processing of conductive materials. A decade ago, $\text{Li}_4\text{Ti}_5\text{O}_{12}$ and LiFePO_4 inks were 3D-printed to serve as the anode and cathode electrodes in a lithium-ion battery, respectively, utilizing the 3D direct printing technique. Nevertheless, the electrodes needed to be heated to $600\text{ }^{\circ}\text{C}$ in an inert gas to remove organic additives and promote nanoparticle sintering.^[17] It is worth mentioning that there is an electrohydrodynamic (EHD) printing technique that has a very high printing resolution (feature sizes of $\approx 240\text{ nm}$ to $5\text{ }\mu\text{m}$) that enables low-temperature processing.^[18] Schneider et al. realized gold mesh with a sheet resistance of $8\text{ }\Omega\text{ sq}^{-1}$ when annealed at $400\text{ }^{\circ}\text{C}$, and Jang et al. achieved silver (Ag) mesh with a sheet resistance of $4.87\text{ }\Omega\text{ sq}^{-1}$ after annealing at $200\text{ }^{\circ}\text{C}$ under near-infrared (NIR) while depositing nanoparticle-based inks.^[19,20] However, since EHD printing relies on an electric field applied between a conductive nozzle and a conductive substrate, the print scale is limited by the distance between the tip of the nozzle and the substrate (i.e., stand-off height) thus 3D structuring is not easy to be realized.^[21] The improved electric-field-driven (EFD) technique enables 3D printing by removing the ground electrode resulting in a larger stand-off height.^[22] EFD has been used to fabricate a 3D-printed Ag mesh with a sheet resistance of $0.75\text{ }\Omega\text{ sq}^{-1}$ when treated at $135\text{ }^{\circ}\text{C}$, and transparent glass heaters based on these metal grids were also developed.^[23–26] However, because of its extremely high printing resolution, printing large-scale 3D objects would be time consuming and would require inks with high solid content.^[24]

Among 3D printing techniques, digital light processing (DLP) has provided a way to fabricate complex, multi-material, or multifunctional objects with high accuracy and resolution in a bottom-up layer-by-layer fashion.^[27–31] DLP relies on the selective

photopolymerization of a liquid photoresin by UV light.^[32–34] To produce conductive structures, Fantino et al. utilized a mixture of a photoresin and Ag nitrate. In this approach, the cross-linking of the polymer matrix and the formation of Ag nanoparticles via photoreduction of the Ag cations took place simultaneously under UV illumination. 3D conductive objects with complex structures were successfully printed however their optimal resistance was limited to $500\text{ k}\Omega$.^[35] Later on, Mu et al. replaced the metal salts with carbon nanotubes achieving a resistance of $\approx 120\text{ k}\Omega$.^[36]

With the rapid development of DLP technology, a variety of advanced photocurable resins have been developed, which greatly expands the functionality and application scenarios of 3D-printed structures. Among them, 3D-printed nanoporous (NPO) structures have aroused our great interest in environmental monitoring, biomedical applications, and catalytic reaction due to their large surface area.^[37–41] NPO materials have been widely used as a host matrix for functional materials including metal nanoparticles, metal salts, metal–halide perovskites, and biological materials such as cells in a large variety of fields.^[42–45] Demchyshyn et al. successfully tuned the bandgap of perovskite in porous films based on the NPO structured templates leading to the precise controlling of the emission wavelength of NPO perovskite nanocrystal light-emitting diodes (LEDs),^[44] which boosts the applications of NPO structures in optoelectronic devices. Lacey et al. directly 3D printed porous graphene oxide as a cathode in a lithium–oxygen battery. The porosity of graphene oxide significantly enhanced the performance of this battery by increasing the access of oxygen and the electrolyte to the whole structure to fully utilize active sites as well as to improve mass/ionic transport.^[45] In addition, these functional electronic devices usually contain a variety of different materials, which means that different techniques could be required to achieve multi-material 3D printing deposition. Incorporating two or more printing technologies such as direct ink writing, aerosol jet printing, inkjet printing, stereolithography printing, DLP printing, etc. has recently shown promising advances in the multi-material 3D printing of multifunctional structures.^[46–50] Thus, combining NPO material systems with additive manufacturing technology such as DLP would offer tremendous potential for novel applications.^[51–53]

In this work, we combined DLP and inkjet printing as an effective strategy to fabricate customized 3D-printed NPO conductive structures. In our approach, the NPO polymeric material is used as a substrate onto which we inkjet-printed a nanoparticle-based Ag ink. By optimizing the deposition conditions, we achieved conductive structures with sheet resistance $< 2\text{ }\Omega\text{ sq}^{-1}$ when annealing at temperatures as low as $100\text{ }^{\circ}\text{C}$. Scanning electron microscope (SEM) and X-ray nano computed tomography (nanoCT) measurements showed that the porous morphology of the pristine NPO was retained after the deposition and annealing of the Ag ink. Finally, we investigated the integration of an inkjet-printed photodetector based on an organic semiconductor active layer onto the NPO substrate. Thus, we demonstrated the potential of this approach for the additive manufacturing of functional 3D-printed optoelectronic devices.

2. Results and Discussion

Figure 1a–d shows the Ag ink infiltration process utilized to fabricate conductive structures based on 3D-printed NPO materials.

R. Debastiani
Karlsruhe Nano Micro Facility (KNMFi)
Karlsruhe Institute of Technology (KIT)
Hermann-von-Helmholtz-Platz 1, 76344 Eggenstein-Leopoldshafen,
Germany

Y. Li, U. W. Paetzold, U. Lemmer, G. Hernandez-Sosa
Institute of Microstructure Technology (IMT)
Karlsruhe Institute of Technology (KIT)
Hermann-von-Helmholtz-Platz 1, 76344 Eggenstein-Leopoldshafen,
Germany

P. Gumbsch
Fraunhofer Institute for Mechanics of Materials IWM
Wöhlerstrasse 11, 79108 Freiburg, Germany

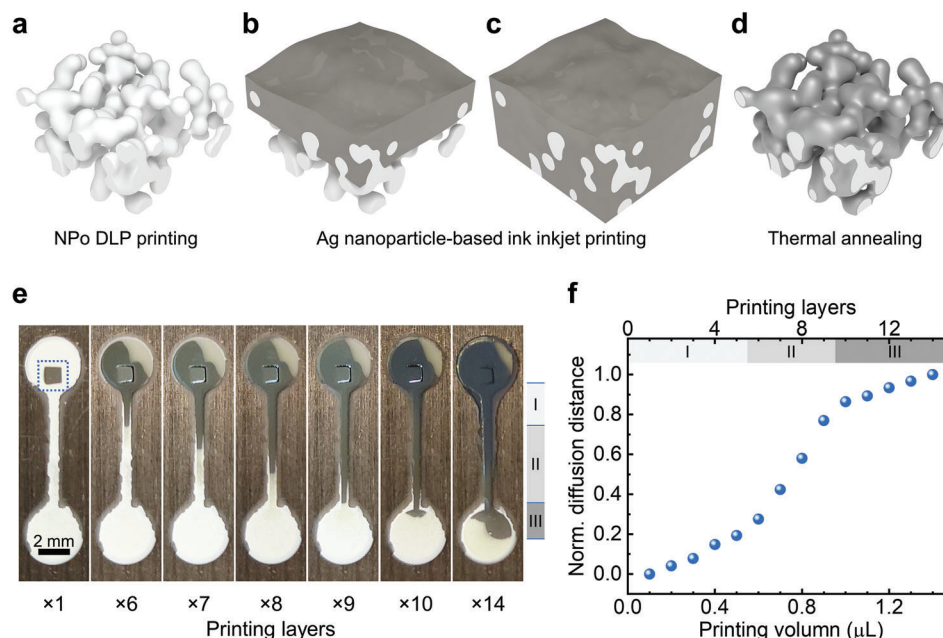


Figure 1. Diffusion of Ag ink in 3D-printed NPo structures. Schematic diagrams of a) pristine NPo structure, b) a small amount of Ag ink onto NPo structure, c) a large amount of Ag ink onto NPo structure, and d) conductive Ag/NPo structure after annealing. e) Photographs of the diffusion of Ag ink in the NPo dumbbell pattern as the number of printing layers increases. f) Normalized diffusion distance of Ag ink in an NPo dumbbell pattern as a function of printing volume and printing layers.

The NPo polymeric matrix was fabricated by DLP printing while the Ag ink was dispensed by inkjet printing before an annealing step. We utilized 2-hydroxyethyl methacrylate (HEMA) and ethylene glycol dimethylacrylate (EDMA) as monomers while Iracure 819 was selected as a photoinitiator due to its high molar extinction coefficients particularly at the UV region.^[33] The key to generating pores is the use of a mixture consisting of cyclohexanol and 1-decanol in our photoresin formulation.^[37,54,55] We furthermore introduced 1-phenylazo-2-naphthol (Sudan I) to reduce the penetration depth of UV light in the resin and obtained a finer structure and improve the printing resolution.^[56] After printing, the completed 3D model was immersed in acetone to remove the uncured resins before the CO_2 supercritical drying process that helps to avoid the collapse of the pores.

By using a DLP printer, we can easily customize the printed objects. A dumbbell-shaped pattern with a thickness of $50\ \mu\text{m}$ was 3D-printed to explore the diffusion of Ag ink into the NPo structure. In Figure 1e, it can be observed that Ag ink can be absorbed and guided through the NPo dumbbell pattern for distances $>1\ \text{cm}$. The Ag ink was subsequently printed in a $1\ \text{mm}^2$ area (blue dotted line box) at a resolution of 2540 dpi. As the number of printed layers increased, it is visible that the Ag ink diffused to the other side of the dumbbell NPo pattern. Figure 1f shows that the diffusion distance has a linear relationship to the deposited ink volume. The different slopes correspond to the filling of the circular structures and the interconnecting bar.

To investigate the conductivity of the printed Ag patterns, we deposited layers with a size of $6\ \text{mm} \times 1.5\ \text{mm}$ at different printing resolutions on top of 3D-printed NPo substrates. To render the patterns conductive, the substrates were then annealed at $100\ ^\circ\text{C}$ for 10 min to evaporate the solvent and sinter

the Ag nanoparticles (for convenience of description, the region where the Ag ink covered the NPo structure will be referred to as “Ag/NPo” hereinafter). A photograph of three of the patterns can be seen in Figure 2a. The measured sheet resistance as a function of the number of printed layers and printing resolution is shown in Figure 2b. When printing at a resolution of 508 dpi, we could only observe low resistance when printing multiple layers. The main reason is that at this resolution the printed Ag ink presents a discontinuous dot pattern (Figure S1, Supporting Information) which is only bridged after the diffusion of more ink. After depositing 20 layers, the average sheet resistance reached $1.94 \pm 0.30\ \Omega\ \text{sq}^{-1}$, which is comparable to that of Ag ink printed on a glass reference substrate. Similarly, for 1016 dpi, the sheet resistance decreased dramatically as the number of printing layers increased. However, when printing with a resolution of 2540 dpi, we achieve a sheet resistance of $3.08 \pm 0.74\ \Omega\ \text{sq}^{-1}$. In contrast to a conductive film printed on glass, the Ag/NPo films require an interlinked 3D network structure, relying on the sintered Ag nanoparticles to form conductive pathways. During the printing process of Ag ink, we observed that at lower ink dosages the Ag ink only partially diffused inside the NPo films as schematically shown in Figure 1b. As the amount of Ag ink increased, the Ag ink went deeper inside the NPo films until it finally covered the whole structure and reached the bottom of the substrate as illustrated in Figure 1c. Figure S2 (Supporting Information) shows photographs of Ag/NPo patterns evidencing this process.

In addition to precisely controlling the amount of Ag ink by selecting the printing resolution and the number of deposited layers, inkjet printing offers additional advantages for the digital design of conductive patterns. Figure 2a (bottom) shows a cat-shaped pattern inkjet-printed onto an NPo substrate at a

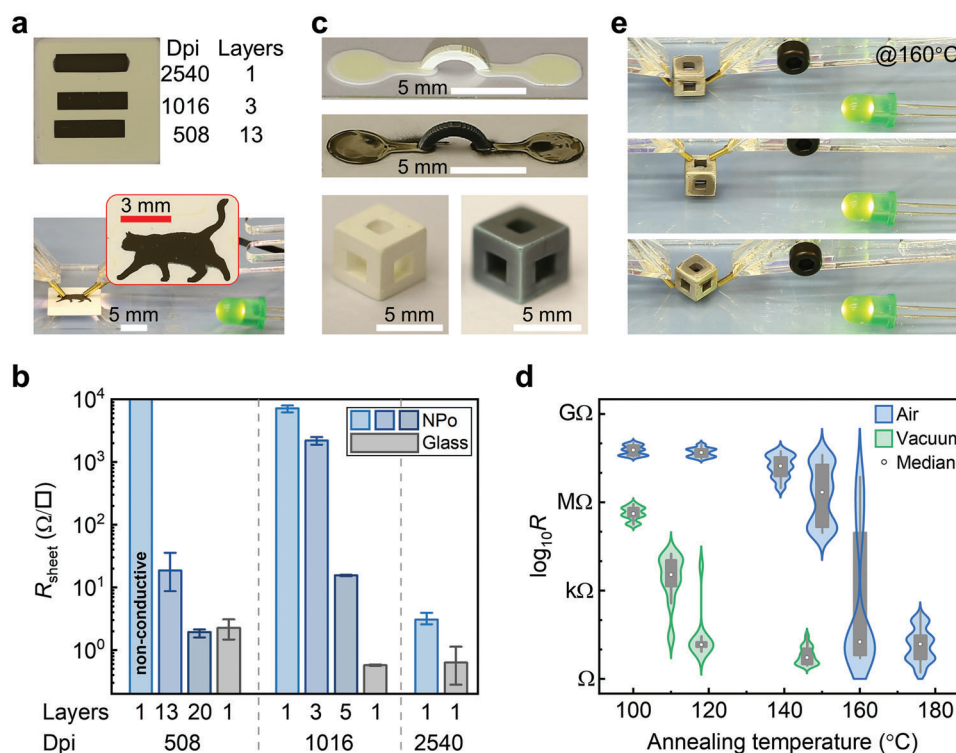


Figure 2. Conductive NPo structures. a) Photographs of rectangles and a cat pattern printed with Ag ink and a demonstration of the conductive cat pattern (CC0 license). b) Sheet resistance of rectangles printed at different print resolutions and with various print layers by averaging three measurements. c) Photographs of 3D-printed NPo bridges and NPo cubes before and after being filled with Ag ink and annealed. d) Resistance of cubes annealed in air and vacuum at different temperatures. The violin plot circles, thick gray bars and thin gray lines correspond to the median, interquartile range (IQR, 25th–75th percentile) and $1.5 \times \text{IQR}$, respectively. e) Photographs of the demonstration of different positions of an NPo cube in the circuit.

resolution of 1016 dpi (4 layers). By using the homemade setup shown in Figure S3 (Supporting Information), we demonstrated that this cat pattern is capable of conducting electrical current and closing the electrical circuit that powered an LED.

To further investigate the fabrication of conductive 3D-printed structures, we investigated the deposition of Ag ink onto millimeter-scale objects. Figure 2c shows 3D-printed NPo structures representing a bridge and a six-way cube ($5 \times 5 \times 5 \text{ mm}^3$), which were infiltrated with Ag ink. Although the pristine NPo cubes printed from the polymer materials appear brittle, we found that they could withstand $\approx 1.2 \text{ kg}$ of weight and remain intact (see Figure S4, Supporting Information). For the bridge structure, we utilized the same process used for the dumbbell structures in Figure 1e and the rectangular patterns in Figure 2a, resulting in a conductivity of $6.24 \pm 3.53 \Omega$. We also succeeded in inkjet printing conductive patterns to functionalize the surface of the six-way cube (see Figure S5, Supporting Information), however, due to its large volume compared to that of the drop volume dispensed by the inkjet printer (i.e., 10 pL), we opted for a dip coating process that would enable a uniform coating. For this, we immersed these NPo cubes in an Ag ink bath for $\approx 4 \text{ min}$ (see Figure S6a–c, Supporting Information). For the annealing step, we threaded a thin wire through the cube and placed it on a homemade sample holder (Figure S6d, Supporting Information) that enables a more homogeneous temperature distribution around the cubes when placing them in an oven (Figure S6e, Supporting Information).

To optimize conductivity, we studied the annealing process of these Ag/NPo cubes in air and vacuum at different temperatures (Figure 2d). Whether annealed in air or vacuum, their resistance values decrease with the increase in annealing temperature. For the samples annealed in air we observed that the median value of the resistance drops from 59.77 M Ω to 15.71 Ω when increasing the temperature from 100 to 176 °C. When annealed in vacuum, the resistance values of the Ag/NPo cubes are significantly lower than those of the Ag/NPo cubes annealed in air at the same temperature. At 100 °C, the resistance of the cube is between 0.1 M Ω and 1 M Ω reaching a minimum mean value of $7.98 \pm 6.60 \Omega$ at 146 °C. In both cases, the data distribution is larger during the transition from high to low resistance that should correspond to the point where the solvent evaporates and the sintering of the Ag nanoparticles. Exemplary photographs of NPo cubes that underwent annealing are shown in Figure S7 (Supporting Information). It is observed tendency to form more cracks in the vacuum-annealed samples even if show higher conductivity. This suggests that vacuum intensifies the volatilization of the Ag ink solvent but affects the structural integrity of the cube more drastically than annealing in air. Figure 2e demonstrates the good conductivity of a 3D-printed six-way cube annealed at 160 °C in air. The cube is capable of closing the electric circuit that powered an LED regardless of the orientation in which it is contacted by the probes.

We furthermore investigated the micromorphology of the NPo and Ag/NPo regions. Figure 3a shows an optical micrograph of the boundary between the pristine NPo region and the Ag/NPo

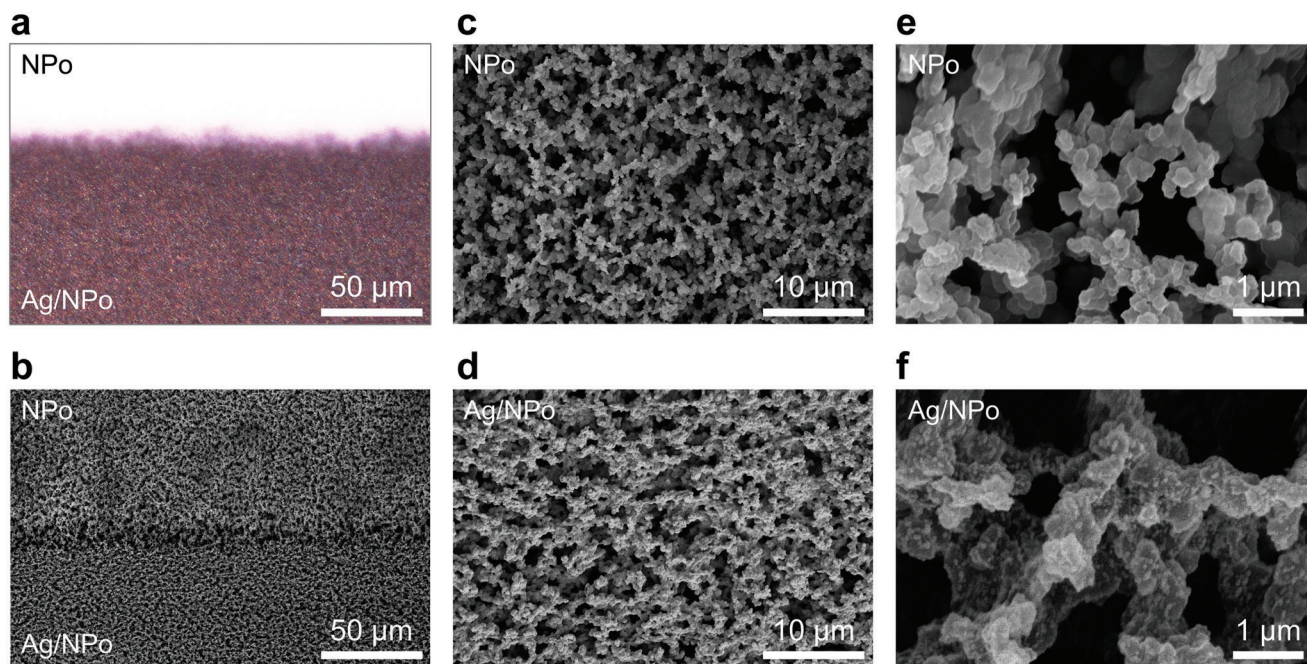


Figure 3. Surface morphological characterization of NPo and Ag/NPo films. a) Microscope graph and b) SEM image of the interface region between NPo and Ag/NPo regions. SEM images of c) NPo film and d) Ag/NPo film at high magnification. SEM images of e) NPo film and f) Ag/NPo film at higher magnification.

region for a sample printed at 1016 dpi (3 layers). It can be seen that the edge of the Ag/NPo area is not a sharp line. The top-view SEM image presented in Figure 3b, shows that the porous morphology of the pristine NPo film is retained after deposition and annealing of the Ag ink. However, the boundary line between the NPo part and Ag/NPo part presents a step. The profilometer and SEM measurements shown in Figure S8 (Supporting Information) indicate that the volume loss in the areas where Ag ink was deposited can be correlated to the amount of ink deposited (e.g., number of layers and/or printing resolution). The step height varies between 8 and 10 μm . With further zooming in, more details about NPo film and Ag/NPo film can be seen in Figure 3c–f. Compared to the pristine NPo film, the Ag/NPo film appears to be denser than the NPo film without losing the 3D network morphology. Comparing Figure 3e and Figure 3f, we can see that Ag seems to form a homogeneous coating around the polymeric matrix effectively reducing the pore size of the structure. This Ag coating seems to be a form of 3D interconnected nano- and micro-particles that are responsible for the observed conductivity of the structures. Through the top-view morphology characterization, we conclude that the Ag ink can diffuse in the NPo films with the increase of printing volume and finally cover the printed area completely while retaining the porosity of the substrate.

Other than the top-view SEM images in Figure 3, we continued to study the internal structure of Ag/NPo films. Through the cross-sectional SEM image of Ag/NPo film in Figure 4a,b, it can be found that the porosity of the entire Ag/NPo film is in the vertical direction all the way until the supporting glass substrate is preserved. At high image magnification (Figure 4c), we clearly observe the sintered Ag particles attached to the NPo material are present throughout the bulk of the material. These cross-

sectional samples were prepared by mechanically cutting the substrate. Similar morphology was also observed in SEM images obtained utilizing a focused ion beam (FIB) cutting (see Figure S9, Supporting Information).

In addition, we investigated the internal structure by nanoCT.^[57] In this technique the sample is scanned nondestructively by an X-ray beam, acquiring 2D projections over 180°. The resulting 3D model is then reconstructed with a filtered back projection algorithm software. The data visualization and segmentation are carried out with the help of commercial software.^[58] The reconstructed 3D structure of an NPo sample is shown in Figure 4d and Video S1 (Supporting Information), while an exemplary slice on the yz plane view is presented in Figure 4e. An example of the xy plane view located in the middle of the 3D NPo model is shown in Figure S10a (Supporting Information). The presented data set shows clearly the internal porous structure of NPo before the deposition of Ag ink. Figure 4f shows the reconstructed 3D Ag/NPo model for a region of the same substrate where Ag was deposited. Its porous structure is also obvious (Video S2, Supporting Information), while its internal structure seems to be denser than that of NPo structures consistent with the results from the SEM images in Figure 3. Similarly, utilizing slices in the zy -plane view (and xy -plane view) such as the one shown in Figure 4g (and Figure S10b, Supporting Information). Cylindrical volumes extracted from the segmented NPo and Ag/NPo data (Figure 4h–k; Figure S11, Supporting Information) show the solid volume ratio for these samples corresponds to 34.75% and 52.88%, respectively. The segmentations confirm the results found with SEM, in which the Ag/NPo film seems to be denser than the NPo film, reducing the pore size of the structure. The reconstructed 3D structure of an interesting

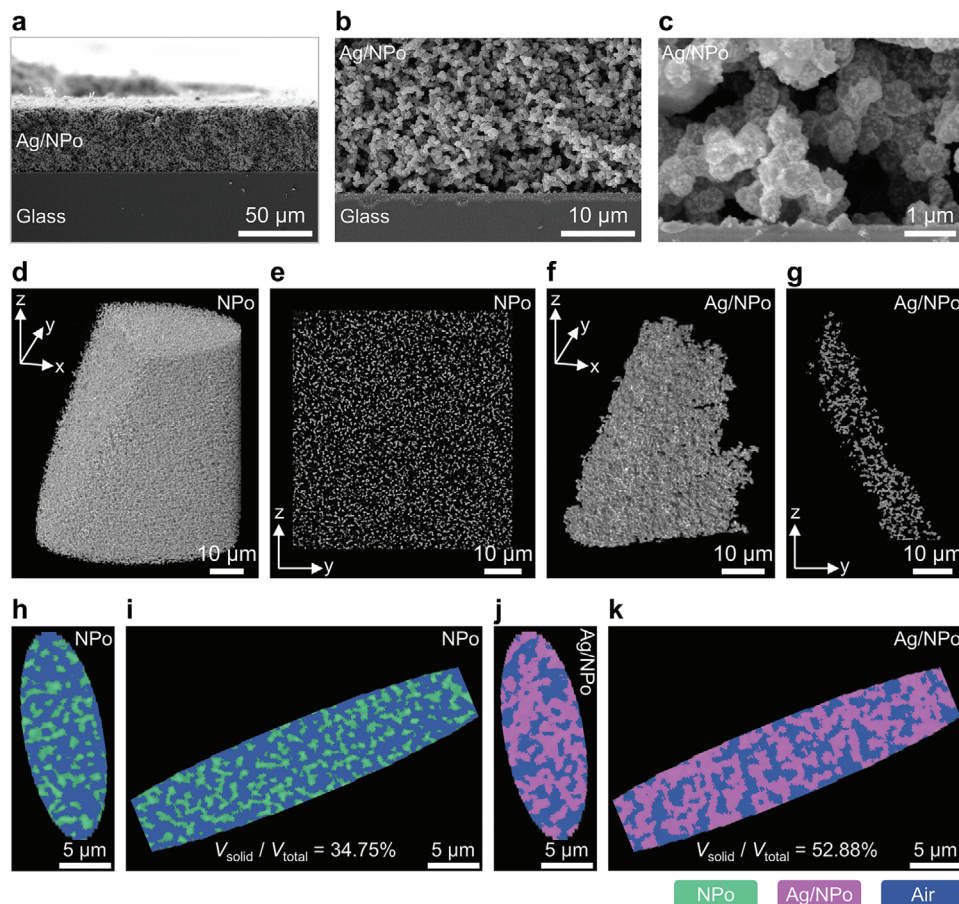


Figure 4. Internal structure characterization of NPo and Ag/NPo structures. a–c) Cross-sectional SEM images of Ag/NPo film at different magnifications. Reconstructed d) NPo 3D model and e) yz plane morphology from nanoCT. Reconstructed f) Ag/NPo 3D model and g) yz plane morphology from nanoCT. Segmented plots of the extracted cylinder of h,i) NPo and j,k) Ag/NPo substrates.

region showing the boundary between NPo and Ag/NPo patterns is shown in Figure S12 and Video S3 (Supporting Information). From this measurement, we can observe a gradual transition region between both domains of $\approx 10 \mu\text{m}$.

In combination with the customizing capabilities of inkjet printing technology, the investigated NPo substrates offer the opportunity to additively integrate patterned electrodes and functional materials into functional optoelectronic devices. **Figure 5** demonstrates the fabrication of an organic photoconductor device onto a 3D-printed NPo substrate. As shown schematically in Figure 5a, the device consists of two electrodes separated by a certain distance (i.e., channel length) bridged by an organic semiconductor material that is responsible for the light to current conversion. We maximize the photoelectric conversion by adopting a highly efficient bulk heterojunction containing so-called donor and acceptor materials in this photoactive layer.^[59,60] Upon light absorption, the generated excitons are dissociated at the interphase between both materials. The resulting electrons and holes from this process are then collected at the electrodes assisted by the applied voltage to form an electrical current. The polymer Poly(3-hexylthiophene-2,5-diyl) (P3HT) and the small molecule 5,5'-[[4,4,9,9-Tetraoctyl-4,9-dihydro-s-indaceno[1,2-b:5,6-b']dithiophene-2,7-diyl]bis(2,1,3-benzothiadiazole-7,4-

diylmethylidene)]bis[3-ethyl-2-thioxo-4-thiazolidinone] (IDTBR) were selected as donor and acceptor, respectively. These two materials were dissolved in chlorobenzene at a weight ratio of 1:1 to obtain a 20 mg mL^{-1} organic solution and deposited by inkjet printing in the same manner as the Ag electrodes.

To characterize the properties of the organic semiconductors deposited in the NPo substrate, we carried out photoluminescence (PL) experiments. Figure 5b shows that pristine P3HT and IDTBR films are strongly luminescent, indicating that the emissive excitonic state at the fundamental gap was not hindered by any detrimental interaction with the substrate material. It can also be observed that the PL of the P3HT:IDTBR sample is strongly suppressed due to the efficient exciton dissociation in this material blend. This provides a positive indication of the photoconversion potential in the device.^[61–63] Since the NPo film is opaque we additionally measured the reflectance spectra of the films (Figure S13, Supporting Information). The pristine NPo substrate has a high reflectance of $\approx 85\%$. After printing P3HT:IDTBR, the reflectance decreased to $<20\%$ indicating efficient light absorption.

The NPo-based organic photoconductors were fabricated by sequentially printing Ag ink and P3HT:IDTBR on the NPo films. Figure 5c shows the photocurrent characteristics of the device as

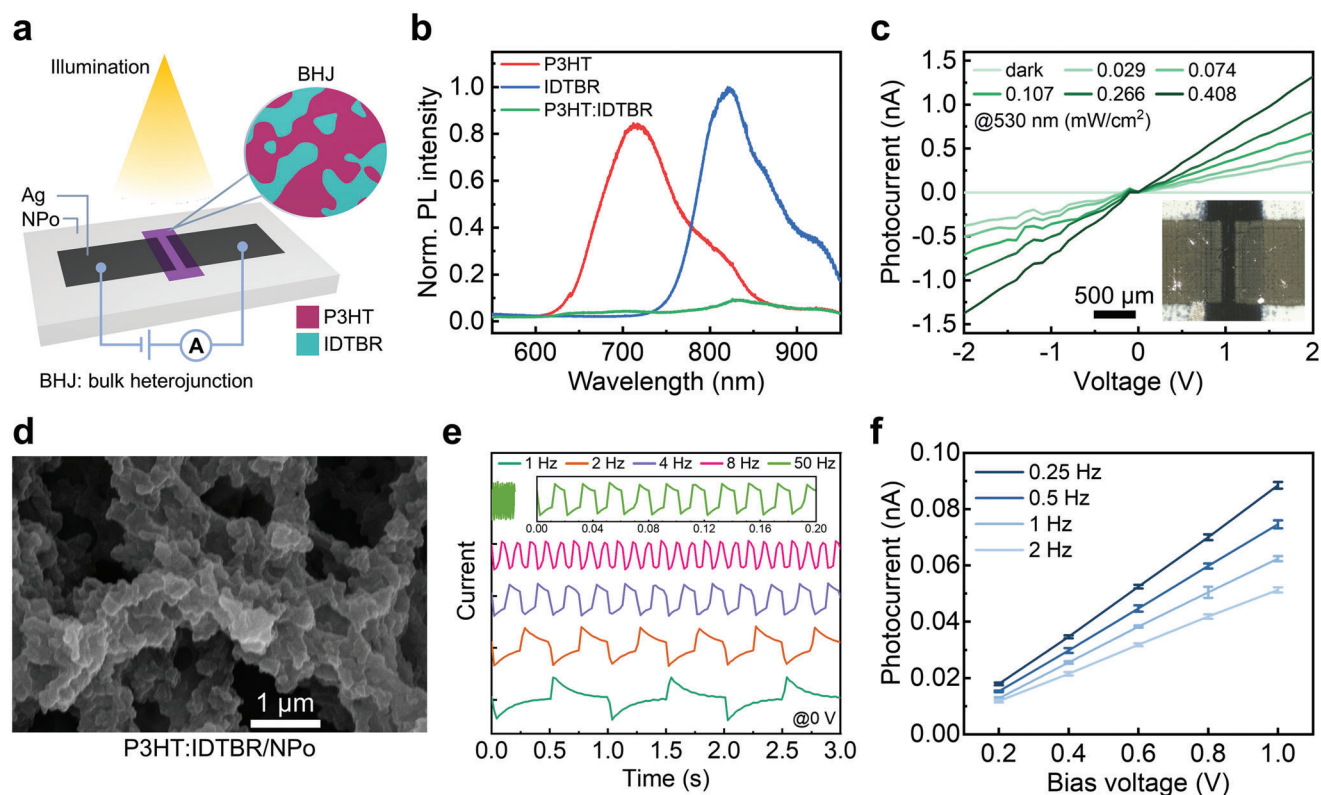


Figure 5. Demonstration and characterization of NPo-based photoconductors. a) Schematic diagram of the photoconductor architecture. b) Photoluminescence spectra of organic semiconductors on NPo films. c) I - V characteristics of NPo-based photoconductors (inset) at different incident light intensities. d) SEM image of the P3HT:IDTBR/NPo region. e) Photoresponse of NPo-based photoconductors under different frequency pulsed light sources. f) Photocurrent versus bias voltage of the detector under incident light of different frequencies.

a function of voltage and incident optical power ($\lambda = 530$ nm). The architecture of the completed device comprising a channel length of $150 \mu\text{m}$ and a channel width of 1 mm is shown in the inset. We can observe a linear increase with higher applied voltage leading to a larger electric field that assists the acceleration and collection of charges at the electrodes. Similarly, by increasing light intensity the device exhibited a maximum photocurrent of 1.38 nA at -2 V .

Typically, the channel length of devices based on photosensitive organic materials is closely related to the collected current in the device.^[64–66] Due to the observed diffusion of Ag ink into the NPo material we chose a channel length of $150 \mu\text{m}$ for sake of reproducibility. In the future, this limit in channel length could be optimized by the viscosity of the ink, porous size or annealing conditions. Current inkjet printing technology could lead to printing resolutions $< 20 \mu\text{m}$.^[67,68] It should be emphasized that the topography of the presented photoactive layer is very different from that of traditional organic thin-film photoconductive devices processed onto flat substrates (e.g., glass). In our case, the annealed organic photoactive layer is wrapped around the NPo structures without closing the pores. This detail is visible in the SEM image of P3HT:IDTBR/NPo film in Figure 5d. Such morphology could be advantageous for the fabrication of gas or humidity sensors based on these kinds of organic materials.^[69,70]

We furthermore investigated the dynamic photoresponse of our device by illuminating it with a pulsed light source. Al-

though their performance is limited by the relatively large channel length, Figure 5e shows that the photoconductor has a good optical response for excitation frequencies up to 50 Hz . Applying bias voltage (Figure 5f), yielded a linear increase in the photocurrent however charging effects could be observed. This can be seen in detail in Figure S14 (Supporting Information) for a set of measurements taken at 1 Hz . The presented photodetector illustrates the feasibility of fabricating inkjet-printed functional devices onto 3D-printed NPo structures. Future work will focus on optimizing its performance by investigating the electronic interface between the metal electrode and the semiconductor and considering geometrical factors during the ink deposition. Additionally, we will address the use of conductive porous structures to interconnect functional devices on the surface of 3D-printed objects.

3. Conclusion

In summary, we demonstrated the fabrication of inkjet-printed conductive structures and the integration of organic optoelectronic devices onto 3D-printed porous materials. We utilized inkjet printing to selectively deposit a nanoparticle-based Ag ink, which could diffuse into the bulk of the DLP-printed NPo substrates. Utilizing a low-temperature ($100 \text{ }^\circ\text{C}$) annealing process, we achieved sheet resistances down to $1.94 \pm 0.30 \Omega \text{ sq}^{-1}$. SEM and nanoCT measurements showed that the porous

morphology of the pristine NPo substrate is retained after the deposition and annealing of the Ag ink. We furthermore showed conductive 3D-printed structures (i.e., six-way cubes) with dimensions $\approx 125 \text{ mm}^3$ showing high electrical conductivity by optimizing a dipping process and annealing post-treatment. Finally, the fabrication of a bulk-heterojunction-based organic photodetector onto the NPo material demonstrated the feasibility of inkjet-printing multi-material functional devices. The results shown herein, are a promising step towards the fabrication of complex systems and functional structures combining digital 3D printing techniques such as DLP and inkjet printing technologies. We expect that the utilized approach could be applicable to the additive integration of other types of functional 3D-printed optoelectronic devices and sensors.

4. Experimental Section

Materials: HEMA, EDMA, Cyclohexanol, 1-decanol, Sudan 1, chlorobenzene, Ag ink (the surface tension, solid content, and viscosity were $35\text{--}40 \text{ dyn cm}^{-1}$, $30\text{--}35\%$, and $10\text{--}18 \text{ cps}$, respectively) and 3-(Trimethoxysilyl)propyl methacrylate were purchased from Sigma-Aldrich. Irgacure 819 was purchased from S u.K Hock GmbH. P3HT ($M_w \approx 58\,000 \text{ g mol}^{-1}$) was purchased from Rieke Metals. IDTBR was purchased from 1-Material. Isopropanol, ethanol, and acetone were purchased from Höfer Chemie GmbH. The ultra-thin glass substrates with a size of $22 \text{ mm} \times 22 \text{ mm} \times 0.18 \text{ mm}$ were purchased from BRAND GMBH + CO KG. All the chemicals were used as received.

Solution Preparation: Photoresin containing 30 wt.% HEMA, 20 wt.% EDMA, 40 wt.% cyclohexanol, 10 wt.% 1-decanol, 4 wt.% Irgacure 819 (with respect to monomers and porogens), and 0.05 wt.% Sudan 1 (with respect to monomers and porogens) was stirred in an ultrasonic bath for half an hour before use. P3HT and IDTBR were dissolved separately in chlorobenzene (20 mg mL^{-1}) and P3HT:IDTBR was prepared by mixing them at 1:1 (volume ratio), they were all stirred overnight to dissolve or mix well.

Fabrication of 3D-Printed Samples: A commercial DLP printer (Miicraft Prime 110) equipped with a UV light source with a wavelength of 405 nm was used to print all NPo structures. Cubes could be printed directly on the platform of the printer. However, extra ultra-thin glass substrates were needed when printing NPo films and bridges. Before attaching the ultra-thin glass substrates to the platform of the DLP printer, they were cleaned sequentially by isopropanol and UV/ozone cleaner (UVO-Cleaner 42–220, Jelight Company Inc.) and then submerged in a mixture of ethanol and 3-(Trimethoxysilyl)propyl methacrylate (25:1 volume ratio) for 4 h, followed by rinsed with ethanol and then blown dry with nitrogen. The photoresin was poured into the tank and then irradiated with the patterned UV light to photopolymerize layer by layer. The printing parameters including the thickness, curing time and etc. are detailed in the attached Table S1 (Supporting Information). After printing, the 3D-printed samples were carefully removed from the platform and then immersed in acetone to remove the non-solid parts. These samples were then preserved in acetone to prevent collapse until being transferred to the chamber of the supercritical apparatus (Leica EM CPD030) for the supercritical drying process by exchanging the solvent with CO_2 . The dried NPo films were used for printed samples later. And the dried NPo cubes were then immersed into Ag ink for 4 min to let ink suck in, followed by hanging up on the homemade shelf and annealing in a vacuum oven (VT 6025, Thermo Scientific) from room temperature to the target temperature at a rate of $\approx 4 \text{ }^\circ\text{C min}^{-1}$, and held for 10 min in air and vacuum, respectively.

Fabrication of Inkjet-Printed Samples: Ag ink and organic solutions were filtered with $0.45 \text{ }\mu\text{m}$ polyvinylidene fluoride (PVDF) filter and $0.2 \text{ }\mu\text{m}$ PVDF filter, respectively, and then were inkjet-printed with an inkjet printer including a $10 \text{ }\mu\text{L}$ DMC cartridge (Diamatix DMP-2850, Fujifilm). The printed samples were then annealed on a hot plate (HS60, Torrey

Pines Scientific) from room temperature to $100 \text{ }^\circ\text{C}$ and then kept at $100 \text{ }^\circ\text{C}$ for 10 min.

Optical Characterization: Reflectance and transmittance spectra of organic semiconductor films on NPo substrates were measured with a UV/VIS/NIR spectrophotometer equipped with a 150 mm InGaAs integrating sphere (Lambda 1050, PerkinElmer) and a custom-built setup including an AvaLight-DHS-Bal light source and a spectrometer (AvaSpec-ULS3648, Avantes), respectively. Steady-state photoluminescence spectra were performed with a fluorometer equipped with a PIXIS 400 CCD (SpectraPro HRS-500, Teledyne Princeton Instruments), in which the excitation light source was a 405 nm CW laser (Thorlabs).

Surface Morphological Characterization: Microscope images were taken with a microscope (Eclipse 80i, Nikon). Profiles of Ag/NPo substrates were measured with a stylus profilometer (Dektak 150, Veeco).

SEM Characterization: SEM images were acquired through a combined focused-ion-beam (FIB)/scanning-electron-microscope (FEI Helios G4 FX, Thermo Fisher Scientific). Before SEM, a thin layer of platinum with a thickness of $\approx 6.2 \text{ nm}$ was sputtered by a sputter coater (EM ACE600, Leica).

NanoCT Characterization: The nanoCT images were obtained with an X-ray microscope (Zeiss Xradia 810 Ultra). The samples were prepared manually by cutting the structures in triangles formats, in which the tip region was scanned with the nanoCT. The samples were scanned using a field of view of $65 \text{ }\mu\text{m}$, Zernike phase contrast mode and a pixel size of 128 nm . 901 projections were acquired over 180° under an acquisition time per projection varying from 5 s for Ag/NPo to 13 s for NPo. The 3D reconstruction of the tomography data was carried out using the proprietary software, based on a filtered back projection algorithm, and Zeiss Scout and Scan Reconstructor. For the 2D and 3D visualization and the segmentation of the data, the software Dragonfly ORS was employed.^[58] The scanned data set of NPo and Ag/NPo samples were filtered using the non-local means filter (kernel 5) previously the segmentation. The manual segmentation was then performed based on the grayscale pixel values. A cylinder of the segmented data was extracted from the middle of each sample, from which the solid ratio was calculated based on the material/air proportion.

Electrical Characterization: Sheet resistance was characterized using a four-point probe station (302 Resistivity Stand with SP4 probe head, Lucas Signatone Corp.) connected to a Keithley 2400 source measure unit (SMU), and the resistance values were obtained from the same SMU. The $I\text{--}V$ measurements were performed with a Keithley 2636A SMU, while illuminated under fiber-coupled LED (M530F2, 530 nm) controlled by the LED Driver (LEDD1B, Thorlabs). The $I\text{--}t$ measurements were also measured with a Keithley 2636A SMU under a 565 nm LED that was triggered by a wave function generator (FG 2102, Voltcraft). The intensities of the light source were measured with an optical power meter (1936-C, Newport) equipped with a calibrated photodiode sensor (818-UV, Newport). A power supply (EA-PS 2084-03 B, EA Elektro-Automatik) was used to demonstrate the good conductivity of the Ag/NPo substrates in the circuit, where the voltage is set to 3 V.

Mechanical Properties Characterization: A small container filled with $\approx 40 \text{ mL}$ of water (total mass of $\approx 68 \text{ g}$) was placed on a single NPo cube. A large container containing $\approx 950 \text{ mL}$ of water (total mass of $\approx 1.12 \text{ kg}$) was then placed on top of the three NPo cubes placed in a triangular shape. Finally, a metal flange weighing $\approx 2.70 \text{ kg}$ was placed on top of these three NPo cubes to further increase the weight, and on top of that was placed the previous large container filled with water for a total mass of $\approx 3.72 \text{ kg}$ (1.24 kg per cube). In the end, these porous cubes remained intact under heavy pressure. An electronic balance (FCB6K0.5, KERN & SOHN GmbH) was used to weigh the water-filled containers and metal flange.

Supporting Information

Supporting Information is available from the Wiley Online Library or from the author.

Acknowledgements

The authors acknowledge the funding from the Deutsche Forschungsgemeinschaft (DFG, German Research Foundation) via the Excellence Cluster “3D Matter Made to Order” (EXC-2082/1-390761711). This work was partly carried out with the support of the Karlsruhe Nano Micro Facility (KNMF, www.knmf.kit.edu), a Helmholtz Research Infrastructure at Karlsruhe Institute of Technology (KIT, www.kit.edu). The Xradia 810 Ultra (nanoCT) core facility was supported (in part) by the 3DMM2O – Cluster of Excellence (EXC-2082/1390761711). P.A.L. thanks DFG (Heisenbergprofessur Projektnummer: 406232485, LE 2936/9-1) for the financial support. S.L. thanks the China Scholarship Council (CSC) for a Ph.D. scholarship. K.X. thanks the Carl Zeiss Foundation for the financial support.

Open access funding enabled and organized by Projekt DEAL.

Conflict of Interest

The authors declare no conflict of interest.

Data Availability Statement

The data that support the findings of this study are available from the corresponding author upon reasonable request.

Keywords

3D printed nanoporous structures, 3D conductive nanoporous structures, digital light processing printing, inkjet printing, organic photoconductors, light detection, nano computed tomography

Received: March 14, 2023

Revised: April 25, 2023

Published online:

- [1] M. A. Gibson, N. M. Mykulowycz, J. Shim, R. Fontana, P. Schmitt, A. Roberts, J. Ketkaew, L. Shao, W. Chen, P. Bordeenthikasem, J. S. Myerberg, R. Fulop, M. D. Verminski, E. M. Sachs, Y. M. Chiang, C. A. Schuh, A. John Hart, J. Schroers, *Mater. Today* **2018**, *21*, 697.
- [2] U. Scheithauer, E. Schwarzer, H. J. Richter, T. Moritz, *Int. J. Appl. Ceram. Technol.* **2015**, *12*, 26.
- [3] J. Y. Lee, J. An, C. K. Chua, *Appl. Mater. Today* **2017**, *7*, 120.
- [4] R. L. Truby, J. A. Lewis, *Nature* **2016**, *540*, 371.
- [5] S. Y. Wu, C. Yang, W. Hsu, L. Lin, *Microsyst. Nanoeng.* **2015**, *1*, 15013.
- [6] M. Mirzaee, S. Noghianian, L. Wiest, I. Chang, presented at 2015 IEEE Int. Symp. on Antennas and Propagation & USNC/URSI National Radio Science Meeting, Vancouver, Canada, July, **2015**.
- [7] S. J. Leigh, R. J. Bradley, C. P. Purcell, D. R. Billson, D. A. Hutchins, *PLoS One* **2012**, *7*, e49365.
- [8] K. Fu, Y. Yao, J. Dai, L. Hu, *Adv. Mater.* **2017**, *29*, 1603486.
- [9] J. H. Martin, B. D. Yahata, J. M. Hundley, J. A. Mayer, T. A. Schaedler, T. M. Pollock, *Nature* **2017**, *549*, 365.
- [10] L. Skoric, D. Sanz-Hernández, F. Meng, C. Donnelly, S. Merino-Aceituno, A. Fernández-Pacheco, *Nano Lett.* **2020**, *20*, 184.
- [11] A. E. Jakus, S. L. Taylor, N. R. Geisendorfer, D. C. Dunand, R. N. Shah, *Adv. Funct. Mater.* **2015**, *25*, 6985.
- [12] T. V. Neumann, M. D. Dickey, *Adv. Mater. Technol.* **2020**, *5*, 2000070.
- [13] U. Daalkhajav, O. D. Yirmibesoglu, S. Walker, Y. Mengüç, *Adv. Mater. Technol.* **2018**, *3*, 1700351.
- [14] N. Hussain, T. Fu, G. Marques, C. Das, T. Scherer, U. Bog, L. Berner, I. Wacker, R. R. Schröder, J. Aghassi-Hagmann, M. Hirtz, *Adv. Mater. Technol.* **2021**, *6*, 2100650.
- [15] D. Foresti, K. T. Kroll, R. Amisshah, F. Sillani, K. A. Homan, D. Poulidakos, J. A. Lewis, *Sci. Adv.* **2018**, *4*, eaat1659.
- [16] Y. G. Park, H. Min, H. Kim, A. Zhembekova, C. Y. Lee, J. U. Park, *Nano Lett.* **2019**, *19*, 4866.
- [17] K. Sun, T. S. Wei, B. Y. Ahn, J. Y. Seo, S. J. Dillon, J. A. Lewis, *Adv. Mater.* **2013**, *25*, 4539.
- [18] J.-U. Park, M. Hardy, S. J. Kang, K. Barton, K. Adair, D. k. Mukhopadhyay, C. Y. Lee, M. S. Strano, A. G. Alleyne, J. G. Georgiadis, P. M. Ferreira, J. A. Rogers, *Nat. Mater.* **2007**, *6*, 782.
- [19] Y. Jang, J. Kim, D. Byun, *J. Phys. D: Appl. Phys.* **2013**, *46*, 155103.
- [20] J. Schneider, P. Rohner, D. Thureja, M. Schmid, P. Galliker, D. Poulidakos, *Adv. Funct. Mater.* **2016**, *26*, 833.
- [21] D. Gao, J. G. Zhou, *Int J Bioprint* **2019**, *5*, 172.
- [22] H. Huang, G. Zhang, W. Li, Z. Yu, Z. Peng, F. Wang, X. Zhu, H. Lan, *Virtual Phys. Prototyping* **2023**, *18*, e2140440.
- [23] X. Zhu, Q. Xu, H. Li, M. Liu, Z. Li, K. Yang, J. Zhao, L. Qian, Z. Peng, G. Zhang, J. Yang, F. Wang, D. Li, H. Lan, *Adv. Mater.* **2019**, *31*, 1902479.
- [24] X. Zhu, M. Liu, X. Qi, H. Li, Y. Zhang, Z. Li, Z. Peng, J. Yang, L. Qian, Q. Xu, N. Gou, J. He, D. Li, H. Lan, *Adv. Mater.* **2021**, *33*, 2007772.
- [25] Z. Li, H. Li, X. Zhu, Z. Peng, G. Zhang, J. Yang, F. Wang, Y. Zhang, L. Sun, R. Wang, J. Zhang, Z. Yang, H. Yi, H. Lan, *Adv. Sci.* **2022**, *9*, 2105331.
- [26] H. Li, Z. Li, N. Li, X. Zhu, Y. Zhang, L. Sun, R. Wang, J. Zhang, Z. Yang, H. Yi, X. Xu, H. Lan, *Small* **2022**, *18*, 2107811.
- [27] C. A. Spiegel, M. Hackner, V. P. Bothe, J. P. Spatz, E. Blasco, *Adv. Funct. Mater.* **2022**, *32*, 2110580.
- [28] C. Vazquez-Martel, L. Becker, W. V. Liebig, P. Elsner, E. Blasco, *ACS Sustainable Chem. Eng.* **2021**, *9*, 16840.
- [29] S. H. Kim, Y. K. Yeon, J. M. Lee, J. R. Chao, Y. J. Lee, Y. B. Seo, M. T. Sultan, O. J. Lee, J. S. Lee, S.-i. Yoon, I. S. Hong, G. Khang, S. J. Lee, J. J. Yoo, C. H. Park, *Nat. Commun.* **2018**, *9*, 1620.
- [30] A. S. Gliozzi, M. Miniaci, A. Chiappone, A. Bergamini, B. Morin, E. Descrovi, *Nat. Commun.* **2020**, *11*, 2576.
- [31] J. Wu, J. Guo, C. Linghu, Y. Lu, J. Song, T. Xie, Q. Zhao, *Nat. Commun.* **2021**, *12*, 6070.
- [32] D. G. Moore, L. Barbera, K. Masania, A. R. Studart, *Nat. Mater.* **2020**, *19*, 212.
- [33] A. Bagheri, J. Jin, *ACS Appl Polym Mater* **2019**, *1*, 593.
- [34] R. J. Mondschein, A. Kanitkar, C. B. Williams, S. S. Verbridge, T. E. Long, *Biomaterials* **2017**, *140*, 170.
- [35] E. Fantino, A. Chiappone, I. Roppolo, D. Manfredi, R. Bongiovanni, C. F. Pirri, F. Calignano, *Adv. Mater.* **2016**, *28*, 3712.
- [36] Q. Mu, L. Wang, C. K. Dunn, X. Kuang, F. Duan, Z. Zhang, H. J. Qi, T. Wang, *Addit. Manuf.* **2017**, *18*, 74.
- [37] Z. Dong, H. Cui, H. Zhang, F. Wang, X. Zhan, F. Mayer, B. Nestler, M. Wegener, P. A. Levkin, *Nat. Commun.* **2021**, *12*, 247.
- [38] F. C. Fierz, F. Beckmann, M. Huser, S. H. Irsen, B. Leukers, F. Witte, Ö. Degistirici, A. Andronache, M. Thie, B. Müller, *Biomaterials* **2008**, *29*, 3799.
- [39] H. Seitz, W. Rieder, S. Irsen, B. Leukers, C. Tille, *J. Biomed. Mater. Res., Part B* **2005**, *74B*, 782.
- [40] C. Zhu, Z. Qi, V. A. Beck, M. Luneau, J. Lattimer, W. Chen, M. A. Worsley, J. Ye, E. B. Duoss, C. M. Spadaccini, C. M. Friend, J. Biener, *Sci. Adv.* *4*, eaas9459.
- [41] M. R. Hartings, Z. Ahmed, *Nat. Rev. Chem.* **2019**, *3*, 305.
- [42] I. Cooperstein, M. Layani, S. Magdassi, *J. Mater. Chem. C* **2015**, *3*, 2040.
- [43] T. Fei, K. Jiang, S. Liu, T. Zhang, *Sens. Actuators, B* **2014**, *190*, 523.
- [44] S. Demchshyn, J. M. Roemer, H. Groß, H. Heilbrunner, C. Ulbricht, D. Apaydin, A. Böhm, U. Rütt, F. Bertram, G. Hesser, M. C. Scharber, N. S. Sariciftci, B. Nickel, S. Bauer, E. D. Glowacki, M. Kaltenbrunner, *Sci. Adv.* *3*, e1700738.

- [45] S. D. Lacey, D. J. Kirsch, Y. Li, J. T. Morgenstern, B. C. Zarket, Y. Yao, J. Dai, L. Q. Garcia, B. Liu, T. Gao, S. Xu, S. R. Raghavan, J. W. Connell, Y. Lin, L. Hu, *Adv. Mater.* **2018**, *30*, 1705651.
- [46] R. B. Wicker, E. W. MacDonald, *Virtual Phys. Prototyping* **2012**, *7*, 181.
- [47] X. Peng, X. Kuang, D. J. Roach, Y. Wang, C. M. Hamel, C. Lu, H. J. Qi, *Addit. Manuf.* **2021**, *40*, 101911.
- [48] D. J. Roach, C. M. Hamel, C. K. Dunn, M. V. Johnson, X. Kuang, H. J. Qi, *Addit. Manuf.* **2019**, *29*, 100819.
- [49] X. Peng, S. Wu, X. Sun, L. Yue, S. M. Montgomery, F. Demoly, K. Zhou, R. R. Zhao, H. J. Qi, *Adv. Mater.* **2022**, *34*, 2204890.
- [50] L. Yue, S. Macrae Montgomery, X. Sun, L. Yu, Y. Song, T. Nomura, M. Tanaka, H. J. Qi, *Nat. Commun.* **2023**, *14*, 1251.
- [51] Z. Dong, M. Vuckovac, W. Cui, Q. Zhou, R. H. A. Ras, P. A. Levkin, *Adv. Mater.* **2021**, *33*, 2106068.
- [52] O. Halevi, T. Y. Chen, P. S. Lee, S. Magdassi, J. A. Hriljac, *RSC Adv.* **2020**, *10*, 5766.
- [53] J. Du, Q. Cao, X. Tang, X. Xu, X. Long, J. Ding, C. Guan, W. Huang, *Chem. Eng. J.* **2021**, *416*, 127885.
- [54] P. A. Levkin, F. Svec, J. M. J. Fréchet, *Adv. Funct. Mater.* **2009**, *19*, 1993.
- [55] D. Lee, F. Svec, J. M. J. Fréchet, *J. Chromatogr. A* **2004**, *1051*, 53.
- [56] J. Muskin, M. Ragusa, T. Gelsthorpe, *J. Chem. Educ.* **2010**, *87*, 512.
- [57] N. Hussain, T. Scherer, C. Das, J. Heuer, R. Debastiani, P. Gumbsch, J. Aghassi-Hagmann, M. Hirtz, *Small* **2022**, *18*, 2202987.
- [58] ORS, Dragonfly (Computer software). Object Research Systems (ORS) Inc, Montreal, Canada **2020**, <http://www.theobjects.com/dragonfly>.
- [59] N. Strobel, N. Droseros, W. Köntges, M. Seiberlich, M. Pietsch, S. Schliske, F. Lindheimer, R. R. Schröder, U. Lemmer, M. Pfanmüller, N. Banerji, G. Hernandez-Sosa, *Adv. Mater.* **2020**, *32*, 1908258.
- [60] K. Xia, Y. Li, Y. Wang, L. Portilla, V. Pecunia, *Adv. Opt. Mater.* **2020**, *8*, 1902056.
- [61] D. Qian, Z. Zheng, H. Yao, W. Tress, T. R. Hopper, S. Chen, S. Li, J. Liu, S. Chen, J. Zhang, X. K. Liu, B. Gao, L. Ouyang, Y. Jin, G. Pozina, I. A. Buyanova, W. M. Chen, O. Inganäs, V. Coropceanu, J. L. Bredas, H. Yan, J. Hou, F. Zhang, A. A. Bakulin, F. Gao, *Nat. Mater.* **2018**, *17*, 703.
- [62] J. J. M. Halls, C. A. Walsh, N. C. Greenham, E. A. Marseglia, R. H. Friend, S. C. Moratti, A. B. Holmes, *Nature* **1995**, *376*, 498.
- [63] P. W. M. Blom, V. D. Mihailetschi, L. J. A. Koster, D. E. Markov, *Adv. Mater.* **2007**, *19*, 1551.
- [64] Y. Peng, F. Guo, H. Xia, W. Lv, L. Sun, S. Xu, H. Zhu, X. Chen, C. Liu, Y. Wang, F. Lu, *Appl. Opt.* **2019**, *58*, 1319.
- [65] J. Han, J. Wang, M. Yang, X. Kong, X. Chen, Z. Huang, H. Guo, J. Gou, S. Tao, Z. Liu, Z. Wu, Y. Jiang, X. Wang, *Adv. Mater.* **2018**, *30*, 1804020.
- [66] T. Birendra Singh, G. Hernandez-Sosa, H. Neugebauer, A. Andreev, H. Sitter, N. S. Sariciftci, *Phys. Status Solidi B* **2006**, *243*, 3329.
- [67] G. Nisato, D. Lupo, S. Ganz, *Organic and Printed Electronics*, CRC Press, Boca Raton, FL **2016**.
- [68] W. Su, B. S. Cook, Y. Fang, M. M. Tentzeris, *Sci. Rep.* **2016**, *6*, 35111.
- [69] F. Zhang, G. Qu, E. Mohammadi, J. Mei, Y. Diao, *Adv. Funct. Mater.* **2017**, *27*, 1701117.
- [70] B. Nketia-Yawson, Y. Y. Noh, *Macromol. Res.* **2017**, *25*, 489.